

# THE JOINT POLARIZATION EXPERIMENT

## Polarimetric Rainfall Measurements and Hydrometeor Classification

BY ALEXANDER V. RYZHKOV, TERRY J. SCHUUR, DONALD W. BURGESS, PAMELA L. HEINSELMAN, SCOTT E. GIANGRANDE, AND DUSAN S. ZRNIC

Advantages of a polarimetric prototype of the WSR-88D radar are confirmed during a demonstration project in Oklahoma.

**R**esearch during the last three decades has demonstrated numerous advantages of dual-polarization radars. For example, polarimetric radars can improve rainfall estimation, better discriminate meteorological and nonmeteorological echoes, and help identify and mitigate the contamination of radar variables by nonweather scatterers. Polarimetric radars have also shown promise in classifying hydrometeors with different microphysical habits and retrieving raindrop size distributions (DSDs), both of which provide insight into storm de-

velopment and precipitation formation. A description of the general principles of weather radar polarimetry and its possible applications can be found in Doviak and Zrnic (1993), Bringi and Chandrasekar (2001), Zrnic and Ryzhkov (1999), Vivekanandan et al. (1999), and Straka et al. (2000), among others.

As part of the continuous modernization of the nationwide network of the Weather Surveillance Radars-1988 Doppler (WSR-88D), the U.S. National Weather Service (NWS) and other agencies have decided to add a polarimetric capability to existing operational radars. The concept was tested on the National Severe Storms Laboratory (NSSL) research and development WSR-88D radar (hereafter referred to as the KOUN radar), to which polarimetric diversity was added in March 2002. The design of the KOUN radar is described in detail by Doviak et al. (2002). A main feature of the radar is that it simultaneously transmits and receives horizontally (H) and vertically (V) polarized waves. A commercial SIGMET RVP7 processor is passively connected to the radar, thereby assuring that there is no effect on normal WSR-88D radar operations. In its simultaneous horizontal and vertical (SHV) transmission and reception mode, the following variables are available: radar reflectivity factor  $Z$  at horizontal polarization, Doppler

**AFFILIATIONS:** RYZHKOV, SCHUUR, BURGESS, HEINSELMAN, AND GIANGRANDE—Cooperative Institute for Mesoscale Meteorological Studies, University of Oklahoma, and NOAA/National Severe Storms Laboratory, Norman, Oklahoma; ZRNIC—NOAA/National Severe Storms Laboratory, Norman, Oklahoma

**CORRESPONDING AUTHOR:** Alexander V. Ryzhkov, NOAA/National Severe Storms Laboratory, 1313 Halley Circle, Norman, OK 73069  
E-mail: Alexander.Ryzhkov@noaa.gov  
DOI:10.1175/BAMS-86-6-809

In final form 30 January 2005  
©2005 American Meteorological Society

velocity  $V$ , spectral width  $\sigma_v$ , differential reflectivity  $Z_{DR}$ , differential phase  $\Phi_{DP}$ , and the magnitude of the cross-correlation coefficient  $\rho_{hv}$  between two copolar components of the radar signal.

In the past year, the NSSL has been conducting an operational demonstration of the polarimetric utility of the KOUN radar. Broadly, this demonstration project, referred to as the Joint Polarization Experiment (JPOLE), has the following objectives:

- Evaluate the engineering design (SHV mode, compatibility with WSR-88D, quality of multiparameter radar data).
- Evaluate the capability to classify meteorological and nonmeteorological scatterers such as hail/rain, rain/snow, insects/birds, etc.
- Validate the quality of rainfall measurements using two gauge networks: Agricultural Research Service (ARS) and Mesonet.
- Deliver radar variables and products (results of classification and rainfall estimation) to the local NWS office for evaluation and feedback.

JPOLE must address three additional issues. First, although the SHV mode has many advantages over the alternate transmission/reception mode (Doviak et al. 2000), the effects on rainfall estimation and hydrometeor classification (due to stronger coupling between two orthogonal components of the radar return) should be determined. It is also important to assess how well the detection of hail, identification of the bright band, and delineation between snow and rain can be made without the linear depolarization ratio—the variable that was historically the first polarimetric parameter utilized for such purposes.

A second issue is the scanning rate used for data collection. Most polarimetric data from previous research studies were collected with relatively slow antenna rotation rates (~1 rpm). This was dictated by the need to reduce and isolate statistical measurement errors from those due to other physical factors. Routine Next Generation Weather Radar (NEXRAD) volume coverage patterns (VCP), however, require at least 3 times higher antenna rotation rates and, therefore, a smaller number of radar samples (or shorter dwell times). Therefore, the algorithms for polarimetric rainfall estimation and classification should be tested with similar VCPs.

Finally, JPOLE must demonstrate the compatibility of the polarimetric WSR-88D prototype with existing operational WSR-88D radars (i.e., it is essential that existing capabilities of the WSR-88D radar are not compromised by the addition of polarization diversity). This requires comparing the quality of nonpolarimetric radar variables (radar reflectivity, mean Doppler velocity, and spectrum width) and products (rain accumulation, probability of hail, etc.) with those obtained from the reference operational radar. The operational KTLX WSR-88D radar, which is approximately 20 km northeast of the polarimetric KOUN radar (Fig. 1), was used as the nonpolarimetric reference radar for these comparisons.

We collected polarimetric KOUN radar data from April 2002 through July 2003. In total, 98 events were catalogued both chronologically and by type, and subsequently described within an online database at <http://cimms.ou.edu/~heinsel/jpole/database.html> and <http://cimms.ou.edu/~heinsel/jpole/stormtype.html>, respectively. Fairly regular real-time delivery of polarimetric radar data and products to the Norman NWS Office began in the fall of 2002. This effort culminated during the JPOLE

intense observation period (IOP) from 15 March 2003 through 15 June 2003. During the IOP, emphasis was placed on providing uninterrupted data delivery to operational forecasters, obtaining extensive forecaster feedback on the use of the polarimetric data in the warning decision process, and collecting high-quality verification datasets that could be used to assess the KOUN radar data and product quality.

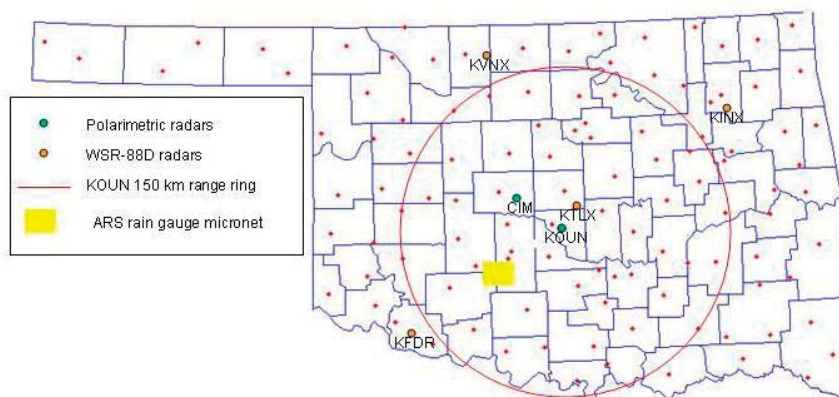


**FIG. 1. Instrumentation for rainfall estimation in Oklahoma. The Mesonet includes 115 gauges with an average gauge spacing of 30 km (Brock et al. 1995); the Microneet consists of 42 gauges with an average gauge spacing of 5 km. Both networks provide 5-min rain accumulation data.**

During JPOLE, data from the polarimetric NSSL Cimarron and conventional NWS KTLX, KINX, KVNK, and KFDR WSR-88D radars, as well as rain gauge data from the Oklahoma Climate Survey (OCS) Mesonet and ARS Micronet, were collected to verify the polarimetric WSR-88D analyses (Fig. 1). Two-hail intercept vehicles and the South Dakota School of Mines and Technology storm-penetrating T-28 aircraft (as part of separate field project) were used for in situ validation results of hail detection and hydrometeor classification during the JPOLE IOP.

The objective of this paper is to give an overview of polarimetric algorithms for rainfall estimation and classification, to illustrate their application for selected events during JPOLE, and to provide a summary of the major results for the whole observational period.

### **POLARIMETRIC RAINFALL ESTIMATION.**

Improvement of quantitative precipitation estimation (QPE) is one of the primary benefits provided by dual-polarization radars. Using multiparameter radar information instead of radar reflectivity alone helps to significantly improve radar data quality, distinguish rain echoes from signals caused by other scatterers (snow, ground clutter, insects, birds, chaff, etc.), and reduce the impact of DSD variability on rainfall estimates. Two polarimetric variables are important for accurate rainfall estimation: differential reflectivity, which is defined as a difference between reflectivities at horizontal and vertical polarizations; and differential phase, which is a difference between the phases of the radar signals at orthogonal polarizations. Differential reflectivity  $Z_{DR}$  is a good measure of the median drop diameter, which should be taken into account for more accurate rain measurements. Among the indisputable advantages of polarimetric rainfall estimation based on specific differential phase  $K_{DP}$  is its immunity to radar miscalibration, attenuation in precipitation, and partial blockage of the radar beam (Zrníc and Ryzhkov 1996).

**Radar dataset.** We have selected two large subsets of radar data for in-depth analysis. The ARS subset consists of 24 rain events with 50 h of observations, during which at least 2 mm of rain fell. This dataset contains 18 convective and 6 stratiform rain events and includes both “warm season” and “cold season” events. Cold-season stratiform rain with a relatively low bright band mostly occurred in October 2002. The Mesonet subset is comprised of 22 rain events and 83 h of observations for the cases observed from August 2002 to June 2003. One hundred and eight

Oklahoma Mesonet gauges were used to validate the results of radar rain measurements at distances between 25 and 290 km from the radar.

The radar variables  $Z$ ,  $Z_{DR}$ ,  $K_{DP}$ , and  $\rho_{hv}$  were estimated using a short dwell time (48 radar samples) in order to satisfy the NEXRAD requirement for a rapid antenna rotation rate (3 rpm) and 1° beam spacing.

**Validation of rainfall algorithms using the ARS Micronet gauges.** The standard WSR-88D  $R(Z)$  relation ( $Z = 300 R^{1.4}$ ) and various polarimetric rainfall algorithms have been validated using the JPOLE dataset. Here we compare the performance of the conventional  $R(Z)$  relation and the best polarimetric algorithm  $R(Z, Z_{DR}, K_{DP})$  (also called a synthetic algorithm) that utilizes three radar variables (see appendix A for more details).

First we examine the performance of the conventional and polarimetric algorithms over the ARS Micronet area. The ARS gauges are between 50 and 88 km from the KOUN radar. At these ranges, DSD variability, raindrop shape uncertainty, and the presence of hail are leading factors that affect the accuracy of rain retrievals. Ground clutter and brightband contamination are usually negligible at these distances from the radar.

We compare 1-h rain totals—both point and areal estimates—obtained from the radar and gauges. By point estimate we mean an hourly total averaged over a small (1–1.5 km) area centered on an individual gauge. Areal mean hourly total (or areal mean rain rate) is determined as a sum of hourly accumulations from all gauges that recorded rain divided by the number of such gauges.

To assess the quality of different polarimetric rain algorithms, we prefer to examine absolute differences between radar and gauge estimates (expressed in mm) rather than standard fractional errors, which are heavily weighted with small accumulations. Rainfall estimates are characterized by the bias  $B = \langle \Delta \rangle$ , standard deviation  $SD = \langle |\Delta - B|^2 \rangle^{1/2}$ , and the rms error  $rmse = \langle |\Delta|^2 \rangle^{1/2}$ , where  $\Delta = T_R - T_G$  is a difference between radar and gauge hourly totals for any given radar–gauge pair, and brackets mean averaging over all such pairs.

An analysis of 24 rain events (50 h of rain) shows that the  $R(Z, K_{DP}, Z_{DR})$  algorithm outperforms the conventional  $R(Z)$  method according to all five statistical criteria: it has the lowest bias, standard deviations, and rms errors for both point and areal rainfall estimates (Table 1). The optimal polarimetric algorithm has a very small overall bias and demonstrates significant reduction of the rms errors (Fig. 2)

**TABLE 1. Mean biases, standard deviations (SD), and rms errors of the radar estimates of 1-h rain totals (in mm) and areal mean rain rates (in mm h<sup>-1</sup>) for the  $R(Z)$  and  $R(Z, K_{DP}, Z_{DR})$  algorithms.**

Algorithms	Point			Areal	
	Bias (mm)	SD (mm)	RMSE (mm)	SD (mm h <sup>-1</sup> )	RMSE (mm h <sup>-1</sup> )
$R(Z)$	1.22	5.16	5.30	3.74	4.02
$R(Z, K_{DP}, Z_{DR})$	-0.01	3.06	3.06	1.09	1.09

compared to the conventional rainfall estimator—1.7 times for point measurements and 3.7 times for areal rainfall estimates.

Figure 3 shows the bias in areal rain rates estimated from radar using the  $R(Z)$  and  $R(Z, K_{DP}, Z_{DR})$  relations versus the hours of observations ranked in chronological order. The two curves in Fig. 3 illustrate overall overestimation/underestimation of rain with both algorithms for different seasons and rain regimes. It is obvious that the conventional algorithm tends to significantly overestimate rainfall associated with intense convection, and especially with hail. The suggested polarimetric method dramatically reduces such overestimation. Both methods slightly underestimate rain for cold-season stratiform events with marginal improvement if the polarimetric algorithm is used (hours 10–30 from October to December 2002).

Of all  $Z$ - $R$  relations, we found that  $Z = 527 R^{1.41}$  yields the smallest rms errors for the point and areal estimates

of rain (4.05 and 2.59 mm, respectively) for the JPOLE dataset. If the polarimetric algorithm is compared to this “optimal”  $R(Z)$ , then the reduction in the rms errors are 1.3 and 2.4 for the point and areal estimates, correspondingly. The optimal  $R(Z)$  relation produces a smaller positive bias for warm season rain events and a significantly larger negative bias for cold season events than does the standard WSR-88D relation. In other words, application of the optimal  $R(Z)$  relation shifts the red curve in Fig. 3 downward without changing its shape. There is not a single  $R(Z)$  relation that matches well the observed rain regimes, whereas the polarimetric algorithm automatically accounts for the differences between various types of rain.

**Evidence of different rain regimes.** JPOLE encountered a large variety of rain regimes characterized by different types of DSD. The  $Z$ - $Z_{DR}$  scattergrams give insight into microphysical properties of rain and the type of DSDs. For a given  $Z$ , very large values of  $Z_{DR}$  generally indicate the DSDs are skewed toward bigger drops, whereas very small  $Z_{DR}$  means a dominance of small drops. A slope of the  $Z$ - $Z_{DR}$  scattergram and its spread are good predictors of rainfall overestimation/underestimation by the  $R(Z)$  relation (Fig. 4).

The rain event on 8 September 2002 (Fig. 4, left side) was associated with a tropical air mass [often characterized by the dominance of small drops in the raindrop spectrum (Ryzhkov and Zrníc 1996)], very “flat”  $Z$ - $Z_{DR}$  scattergrams, and values of  $Z_{DR}$  barely exceeding 1 dB even for reflectivities reaching 50 dBZ. Hence,  $R(Z)$  heavily underestimates rainfall. In the second example, the storm on 14 May 2003 (Fig. 4, right side)

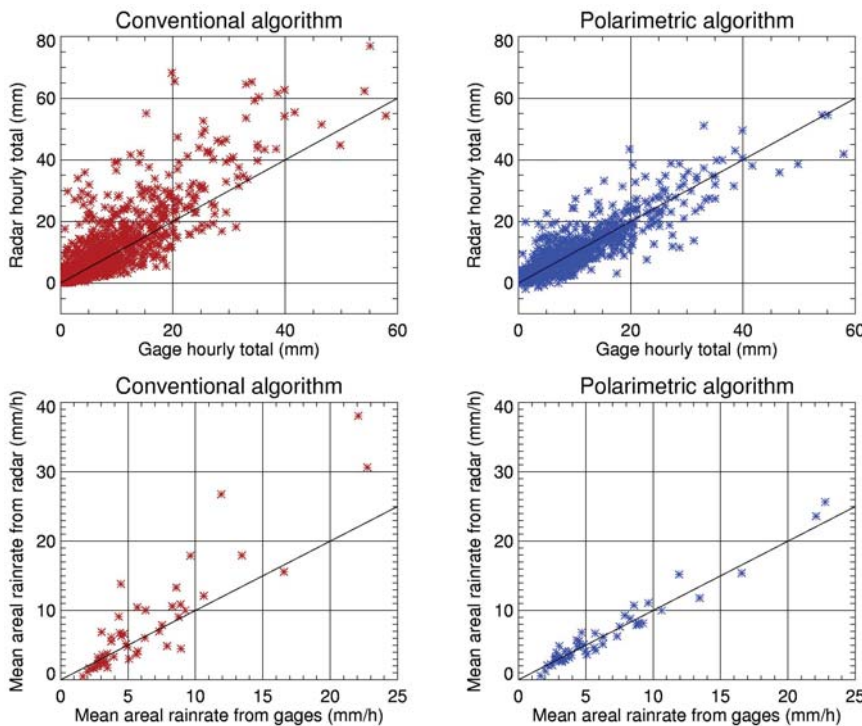


**FIG. 2. (top) One-hour accumulations and (bottom) mean areal rain rates from gauges vs their estimates from the  $R(Z)$  and  $R(Z, K_{DP}, Z_{DR})$  algorithms (24 rain events, 50 h of observations).**

produced intense rainfall (near-flash flood criteria) in the ARS Micronet area and hail exceeding 5 in. in diameter. Some of the Micronet gauges recorded rain rates of about  $200 \text{ mm h}^{-1}$ , and at least three gauges registered hourly rain totals exceeding 2 in. The sharp decrease of  $Z_{DR}$  for  $Z > 60 \text{ dBZ}$  is a clear indication of hail. Hail cores are typically surrounded by regions of very high  $Z_{DR}$  that can be attributed to melting hail or giant raindrops with ice cores inside. The contribution of such areas to the rain total is usually much larger than the contribution from “pure” hail-contaminated regions where high  $Z$  is coupled with low  $Z_{DR}$ .

The  $Z$ - $Z_{DR}$  scattergrams for rain mixed with hail are extremely broad, that is, very high values of  $Z_{DR}$  are observed in a wide range of reflectivities, including very low ones. This explains why thresholding of  $Z$  at a certain level (53 dBZ for the WSR-88D radars) only partially mitigates the impact of hail on the quality of rain measurement. We still observe a substantial overestimation of rain after the 53-dBZ threshold is applied to the radar reflectivity data (Fig. 4, right side). The polarimetric method significantly improves rain estimates in both cases.

Overall, the most significant improvement is achieved in areal rainfall estimation and in measurements of heavy precipitation (often mixed with hail). These advantages have important practical implications for a) river flash-flooding forecasts and management that require reliable measurement of areal rain accumulations regardless of rain intensity, and b) urban flash-flooding forecasts that require the accurate estimation of heavy rain at a high spatial resolution.

*The quality of rainfall estimates as a function of range.* The NWS requires that rainfall be estimated

**FIG. 4.** The  $Z$ - $Z_{DR}$  scattergrams and hourly ARS gauge totals vs their estimates from the  $R(Z)$  and  $R(Z, K_{DP}, Z_{DR})$  algorithms in the cases of (left) tropical rain and (right) rain mixed with hail.

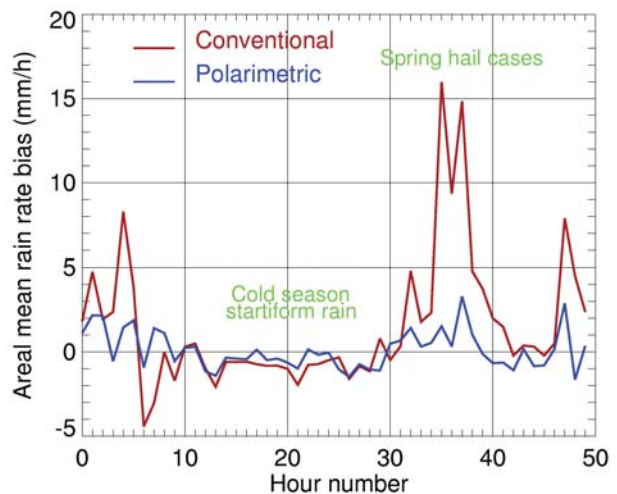
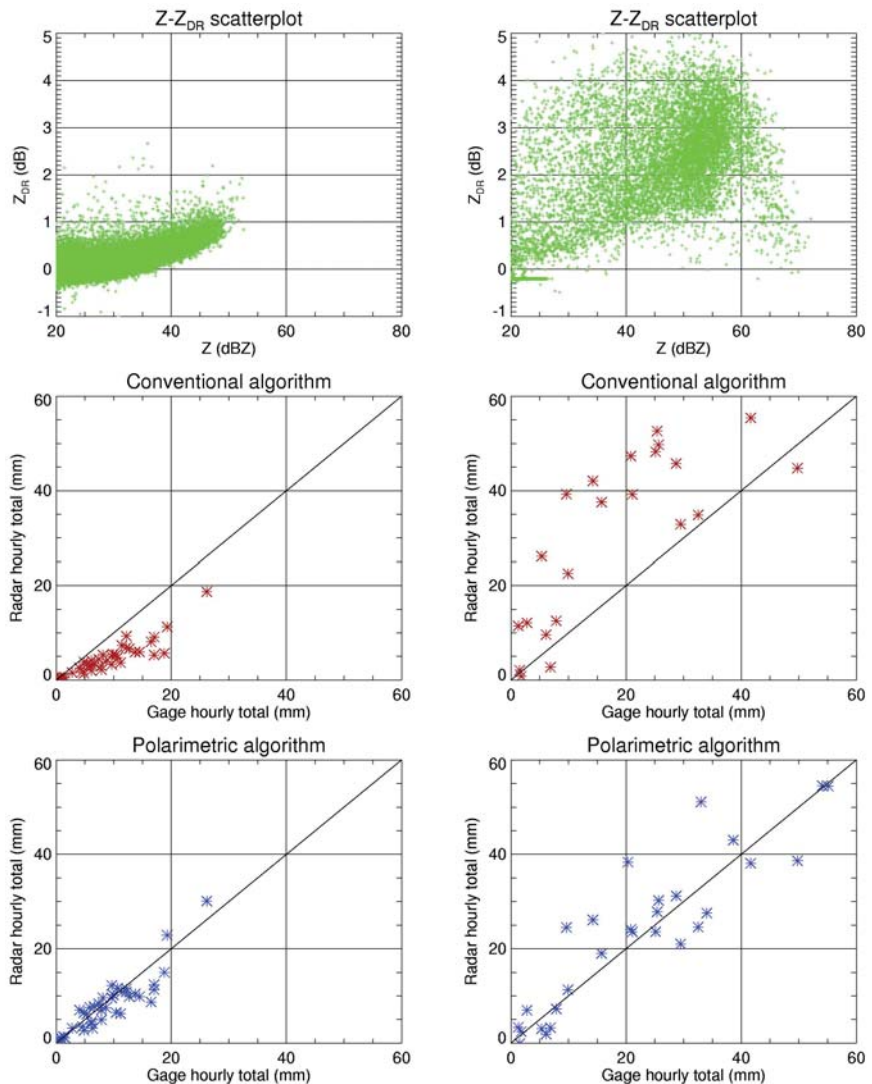


**FIG. 3.** The bias in areal rain rates estimated from radar using the  $R(Z)$  and  $R(Z, K_{DP}, Z_{DR})$  algorithms vs the hour of observations ranked in chronological order.

up to 230 km in range from a radar. While some studies discuss the quality of conventional radar rain estimates at large distances (e.g., Smith et al. 1996; Seo et al. 2000), the performance of polarimetric methods at distances greater than 100 km has not been well investigated. With few exceptions, the majority of the dual-polarization S-band radar–gauge comparisons have been made for warm-season precipitation and at distances of less than 100 km. It was not clear if the advantages of dual-polarization radar for rain measurements hold at larger distances from the radar. Therefore, we used Oklahoma Mesonet rain gauges to validate conventional and polarimetric algorithms for rainfall estimation in a broad range of distances from the radar.

The presence or absence of the bright band affects performance of all radar algorithms at large distances. Separate statistics were obtained for the cold season events, for which the bright band played a significant role, and the warm season events, which were not substantially affected by the bright band. The cold season subset contains 29 h of observation from September through November 2002. Although these events might contain embedded convection, they are best classified as widespread stratiform precipitation and nocturnal events associated with

mesoscale convective systems. The warm season subset includes 54 h of observation from late April to mid-August 2002–03. These rain events are mostly ordinary convective lines with occasional supercells; some have significant portions of stratiform rain. Substantial hail was reported for several warm-season storms.

The mean biases and rms errors of 1-h rain totals were computed in the range interval of 50–225 km and displayed as functions of range (Fig. 5) separately for cold- and warm- season events. Intervals of 50 km in range, centered at 25-km increments beginning with a range of 50 km, have been selected for this analysis. There are a total of 2088 hourly comparisons for the 25–250-km interval representing data from 9 rain events.

At relatively close distances (less than 130 km from the radar) where brightband contamination is negligible, the quality of radar rainfall estimates is mostly determined by DSD variations and the possible presence of hail. As our analysis shows, these two problems are best addressed by the synthetic  $R(Z, K_{DP}, Z_{DR})$  algorithm.

In the range interval of 130–200 km, the bright band becomes a leading factor affecting the performance of all algorithms during the cold season, when

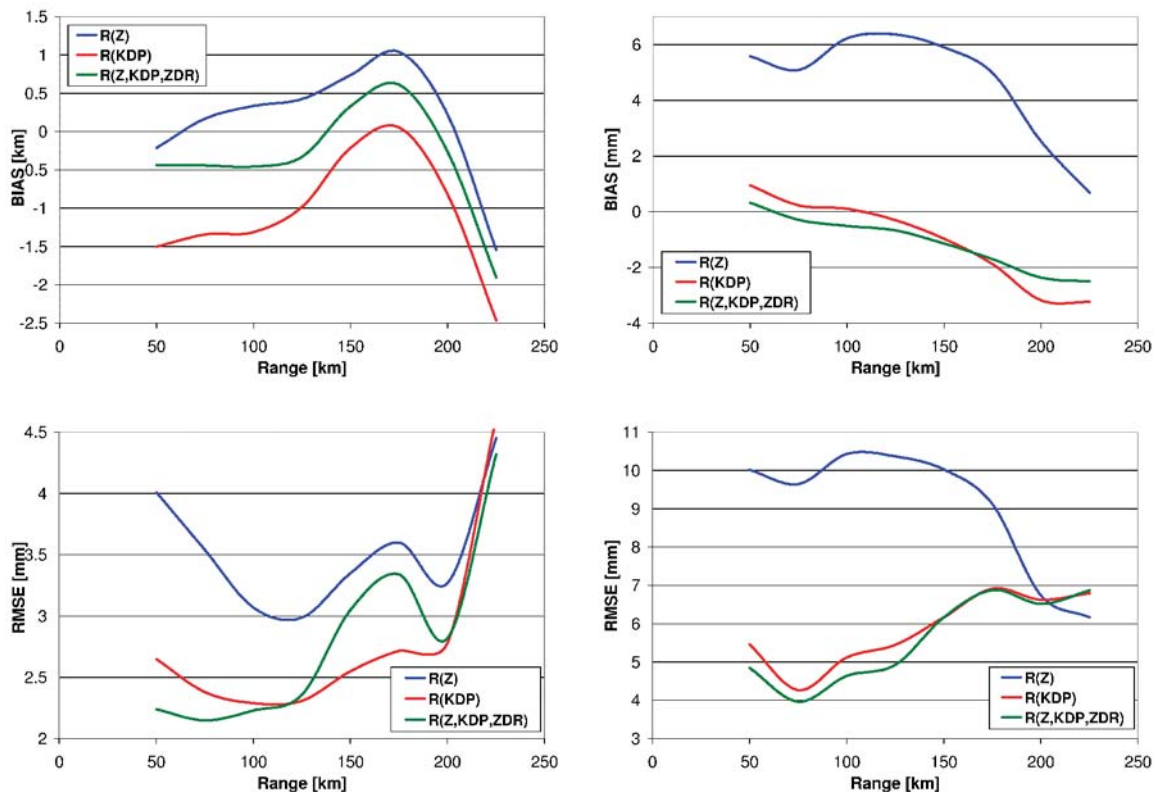


**FIG. 5.** Mean biases and rms errors of the hourly rain totals estimated from different algorithms as functions of range for (left) cold-season and (right) warm-season cases.

rain is predominantly stratiform and the melting level is quite low. At these distances, the synthetic algorithm is no longer superior because  $Z$  and  $Z_{DR}$  are substantially affected by melting hydrometeors. Surprisingly, the  $R(K_{DP})$  algorithm, which solely relies on  $K_{DP}$  (see appendix A), is more immune to the brightband contamination than the others. It performs best of all, both in terms of bias and rms error. The situation is very different in the warm season when rain is mostly associated with strong localized convection—rain fields are very nonuniform, and brightband contamination is not a key factor. Although rain estimates from the  $R(Z, K_{DP}, Z_{DR})$  and  $R(K_{DP})$  algorithms are still the best in terms of the rms error, the corresponding biases become increasingly negative. Possible aliasing of differential phase and nonuniform beam-filling effects are likely causes of such a progressive negative bias. Beyond 200 km, all algorithms perform poorly because of beam-overshooting precipitation, beam broadening, and loss of sensitivity.

In summary, the polarimetric rainfall algorithm, which is based on the combined use of  $Z$ ,  $Z_{DR}$ , and  $K_{DP}$ , clearly outperforms a conventional  $R(Z)$  relation in terms of both bias and the rms error. At distances less than 100 km from the radar, the rms error of the 1-h total estimate is reduced by a factor of 1.7 for point measurements and a factor of 3.7 for areal rainfall estimates. At longer distances, the polarimetric method also provides improved rainfall estimation, although to a lesser degree. The choice between  $R(Z, K_{DP}, Z_{DR})$ ,  $R(K_{DP})$ , or another polarimetric relation depends on the presence or absence of the bright band, which can be identified using a polarimetric classification procedure.

**HYDROMETEOR CLASSIFICATION.** *General principles of classification.* One of the important advantages of polarimetric weather radars is their ability to

discriminate between different types of hydrometeor and nonhydrometeor scatterers. Our classification algorithm is based on the principles of fuzzy logic (Vivekanandan et al. 1999; Zrnica and Ryzhkov 1999; Straka et al. 2000; Liu and Chandrasekar 2000; Zrnica et al. 2001).

Five radar variables have been used for the automatic classification reported herein. These are 1) radar reflectivity  $Z$ , 2) differential reflectivity  $Z_{DR}$ , 3) cross-correlation coefficient  $\rho_{hv}$ , between horizontally and vertically polarized components of the radar return, 4) a texture parameter  $SD(Z)$  of the  $Z$  field, and 5) a texture parameter  $SD(\Phi_{DP})$  of the field of differential phase  $\Phi_{DP}$ . The two latter variables are especially efficient for discrimination between meteorological and nonmeteorological radar echoes. The parameters  $SD(Z)$  and  $SD(\Phi_{DP})$  characterize the depth of small-scale fluctuations of  $Z$  and  $\Phi_{DP}$  along the radar ray.<sup>1</sup>

The classification procedure can be customized according to the user's needs. Depending on the primary task, different sets of radar variables, different classes, and different weights can be used. For example, the algorithm can be optimized either for discrimination between meteorological and nonmeteorological scatterers (meteo versus nonmeteo) or for distinguishing different categories of meteorological echo (e.g., rain versus hail or snow). In JPOLE, we used three different (in substance and complexity) versions of the polarimetric classification algorithm. A list of classes that are identified with the three versions of the fuzzy logic classifier is presented in Table 2.

<sup>1</sup> To obtain  $SD(Z)$ , we average  $Z$  data (sampled every 0.267 km) along the radial using a 1-km running average and subtract the smoothed estimates of  $Z$  from their original values. A similar procedure is used for computing the parameter  $SD(\Phi_{DP})$ , but with a 2-times-wider averaging window.

**TABLE 2.** List of radar echo types identified with three versions of the fuzzy logic classifier.

Version 1: Meteo–nonmeteo	Version 2: Warm season	Version 3: Cold season
Ground clutter/AP: AP	Ground clutter/AP: AP	Ground clutter/AP: AP
Biological scatterers: BS	Biological scatterers: BS	Biological scatterers: BS
Rain: RA	Big drops: BD	Dry aggregated snow: DS
	Light rain: LR	Wet snow: WS
	Moderate rain: MR	Stratiform rain: SR
	Heavy rain: HR	Convective rain: CR
	Rain/hail: HA	Rain/hail: RH

All three versions were designed to filter out radar echoes from nonmeteorological scatterers (ground clutter, birds, insects, etc.)—an important component of data quality improvement and one of the primary advantages of a dual-polarization radar. Version 2 was primarily utilized for warm-season weather events during JPOLE. A category “big drops” describes a raindrop spectrum that is characterized by a relatively substantial number of larger drops and fewer small ones than was encountered in most DSDs. This skewed type of DSD, which is commonly observed in the inflow regions of rapidly developing convection, has an important prognostic value for weather forecasters. Version 3 includes two categories of frozen particles (dry aggregated snow and wet snow) among others, thus, it was a preferred classifier for cold-season events.

*Discrimination between meteorological and nonmeteorological scatterers.* The quality of discrimination between meteorological and nonmeteorological scatterers using version 1 of the classification algorithm is illustrated in Fig. 6. The radar reflectivity image gives limited clues for identification. The classification algorithm, however, identifies extended regions of anomalous propagation (AP) embedded in precipitation. The AP-contaminated areas in Fig. 6 are marked by slightly negative values of  $Z_{DR}$  and a  $\rho_{hv}$  lower than what is typically observed in rain. Regions classified as biological scatterers are characterized by high  $Z_{DR}$  and low  $\rho_{hv}$ .

Although the use of  $\rho_{hv}$  alone yields very good separation of meteorological and biological scatterers, it is not always sufficient to distinguish between weather echoes and ground clutter/AP. The texture

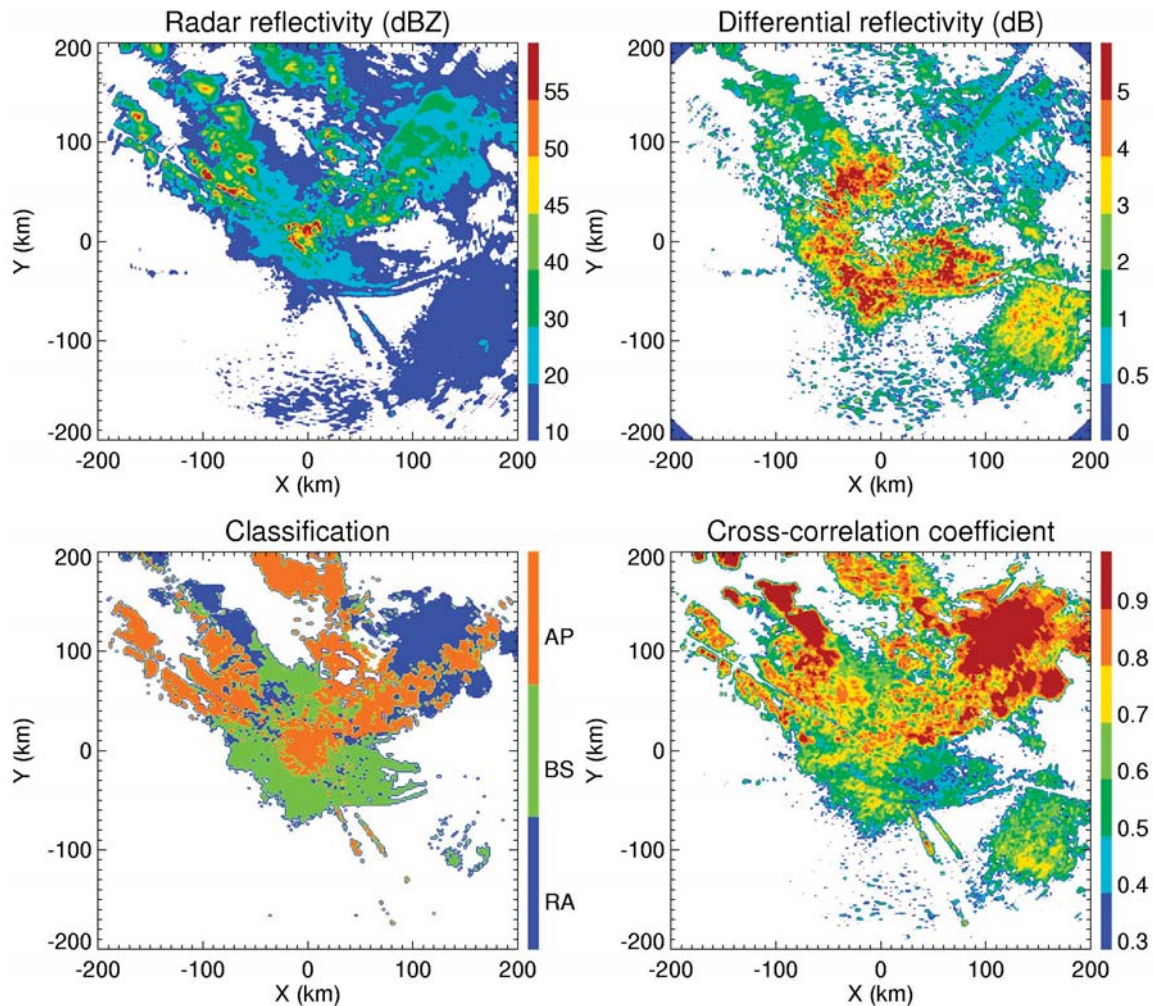


**FIG. 6.** Composite plot of  $Z$ ,  $Z_{DR}$ ,  $\rho_{hv}$ , and results of classification at  $EI = 0.5^\circ$  at 0734 UTC 24 Aug 2002. Here, RA stands for rain, BS for biological scatterers, and AP for ground clutter/anomalous propagation.

parameters  $SD(Z)$ , and especially  $SD(\Phi_{DP})$ , might also be helpful for discrimination between weather and ground echoes (Schuur et al. 2003). Although none of the five radar variables enables perfect delineation among the three classes, their combination in a fuzzy logic approach is very efficient for classification.

The ability of the algorithm to classify meteorological and nonmeteorological scatterers is quantified as follows. We selected eight cases that exhibited extensive areas of radar echo caused by either AP or biological scatterers, and estimated relative proportions of correctly classified and misclassified echoes. We found that the number of 2 km x 2 km pixels (used as a grid interval in our analysis) identified as “non-meteo” in pure rain areas (e.g., in rain at elevation 1.5° without AP echo) was usually less than 1% of the total number of pixels for which the signal-to-noise ratio (SNR) exceeds 10 dB. A similar proportion of misclassification (less than 1%) was found in the opposite situation—“meteo” pixels in the AP areas—provided that SNR is again higher than 10 dB. The quality of classification deteriorates with decreasing SNR (up to 5% of misclassified pixels in several cases if SNR > 5 dB). This deterioration is attributed to the fact that the key polarimetric variables,  $Z_{DR}$  and  $\rho_{hv}$ , are biased by noise and, in these data, can be reliably corrected if SNR > 5–10 dB.

Neither version of the classification algorithm utilized in JPOLE provided discrimination between insects and birds. Nevertheless, recent experimental studies (Zhang et al. 2004) demonstrate the potential capability of the polarimetric radar to distinguish between insects and birds and reveal different diurnal cycles for radar echoes associated with either type of these biological scatterers. Birds are usually characterized by larger values of differential phase upon scattering and a lower differential reflectivity than insects (Zrnica and Ryzhkov 1998; Zhang et al. 2004).

Another type of nonmeteorological radar echo in the atmosphere that can be reliably detected by the polarimetric radar is chaff released by the military. An interesting case of chaff detection during JPOLE is reported by Zrnica and Ryzhkov (2004). The chaff signature is characterized by an anomalously low cross-correlation coefficient (0.2–0.5) and high values of differential reflectivity (up to 6 dB).

**Detection of hail.** The current WSR-88D hail detection algorithm (HDA) estimates hail and severe hail probability, as well as maximum hail size, on the basis of storm structure and environmental factors that are difficult to quantify (Witt et al. 1998). Because

the estimates characterize a whole storm cell, HDA does not specify the actual location of the hail. In contrast, the polarimetric hydrometeor classification algorithm (HCA) determines precise regions of hail within a storm cell by capitalizing on the difference between polarization properties of hydrometeors with different microphysical habits in any given radar resolution volume.

In accordance with the HCA, hail is identified by high values of  $Z$  combined with low  $Z_{DR}$  and  $\rho_{hv}$  (Aydin et al. 1986; Balakrishnan and Zrnica 1990; Smyth et al. 1999; and others). In order to distinguish between hail and ground clutter/AP, which might have a very similar  $Z$ ,  $Z_{DR}$ , and  $\rho_{hv}$ , we also use the texture parameters [ $SD(Z)$  and  $SD(\Phi_{DP})$ ] and Doppler velocity  $V$ . Ground clutter/AP is characterized by low absolute  $V$  and high values of the texture variables. Figure 7 shows HCA results at the 0.5° elevation for the 14 May 2003 supercell that produced hail with a diameter of more than 5 in. (i.e., 12.7 cm). The giant hail that fell from the storm cell at a location of approximately  $X = -10$  km and  $Y = -85$  km is associated with a  $Z$  that exceeded 70 dBZ, a slightly negative  $Z_{DR}$ , and a  $\rho_{hv}$  as low as 0.8. The area classified as big drops in the updraft region at the southern edge of the storm is characterized by a  $Z_{DR}$  exceeding 3 dB and low-to-moderate  $Z$ .

During JPOLE, KOUN data were collected from 18 events that produced polarimetric signatures indicative of hail. Storm-intercept vehicles collected ground-truth data within 150 km of the radar for five of these events: an isolated low-precipitation (LP) supercell storm on 1 May, a classic supercell storm on 19 May, lines of convective storm cells on 14 May and 10 June, and two linearly aligned LP supercell storms on 11 June. To validate hail detection by the conventional (HDA) and polarimetric (HCA) algorithms, the ground truth data were compared with HDA and HCA output. HDA was run using data collected by KTLX, the nearest operational WSR-88D radar (20 km northeast of KOUN). For HDA, probabilities of hail 60% or higher were considered as indicative of hail falling at the ground. Because KTLX data were unavailable for the 11 June event, the evaluation pertains to the other four events only. HCA was run using data collected by the polarimetric KOUN radar. Hail classification at the 0.5° elevation was considered to be indicative of hail falling at the ground.

Ground-truth data included in this validation (47 reports) showed hail sizes from about 0.5 to 4.45 cm, and met a set of temporal and spatial criteria. Each hail report had to occur within  $\pm 6$  min of available radar data (both KOUN and KTLX) and

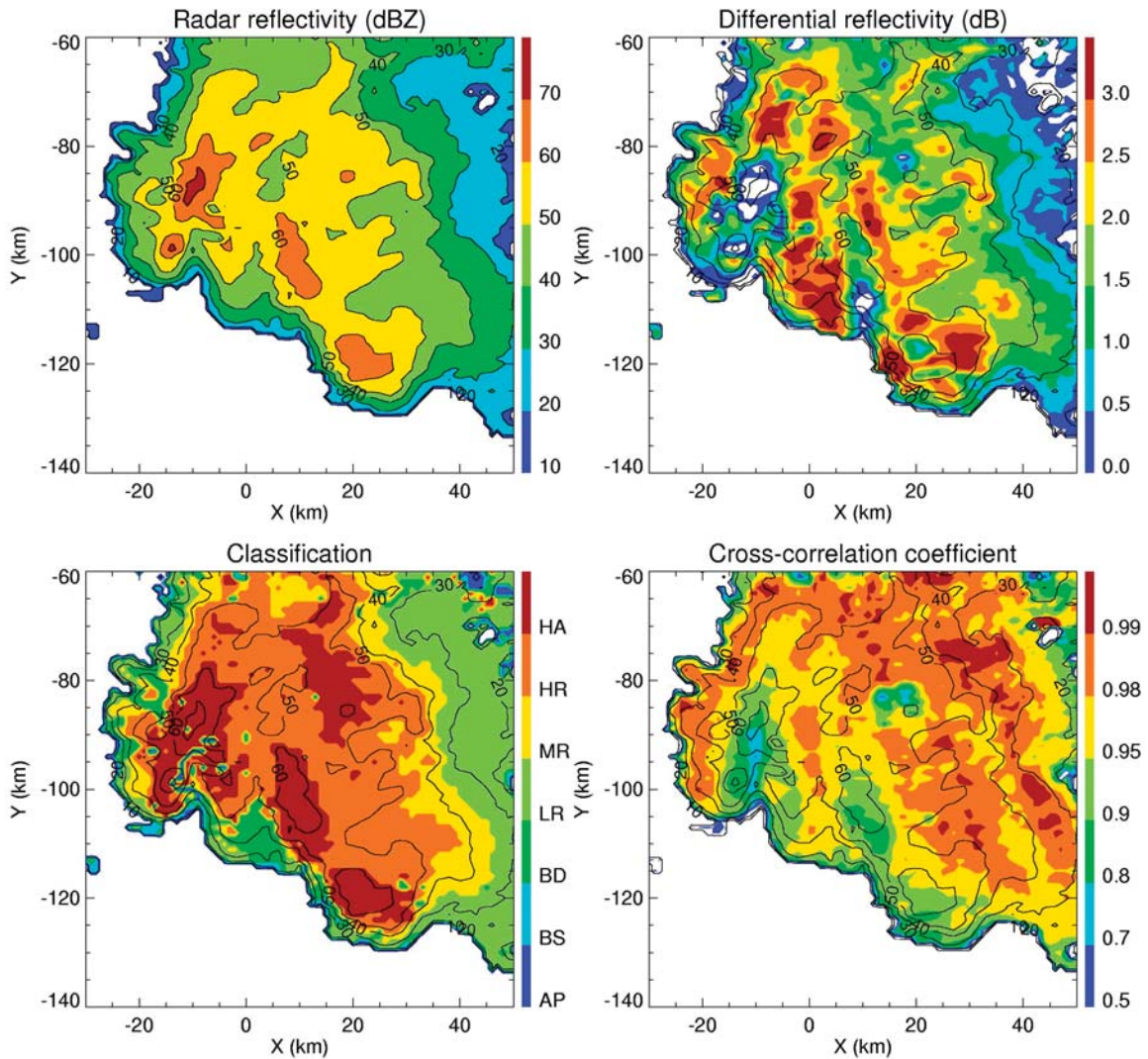


**FIG. 7.** Composite plot of  $Z$ ,  $Z_{DR}$ ,  $\rho_{hv}$ , and results of classification at  $EI = 0.5^\circ$  at 0834 UTC 14 May 2003. AP stands for ground clutter/anomalous propagation, BS for biological scatterers, BD for big drops, LR for light rain, MR for moderate rain, HR for heavy rain, and HA for rain/hail mixture.

be located within an acceptable distance of either the 40-dBZ or higher reflectivity contour or a region classified as hail. This distance, or radius of influence, varied from 3.2 to 5 km, depending on the speed of storm movement.

Using these criteria, a 2 x 2 contingency table was created for all days combined and used to compute the following measures: probability of detection (POD), probability of false detection (POFD), false alarm rate (FAR), critical success index (CSI), and Heidke skill score (HSS; see appendix B for definitions). For the four cases in this study, HCA outperforms HDA in terms of overall accuracy and skill (Table 3). The most striking performance improvements for HCA, relative to HDA, are a 49% increase in HSS and a 33% decrease in POFD. This substantial increase in

HSS means that HCA classifies hail more skillfully than HDA, with respect to a random classification. The substantial decrease in POFD means that HCA is less likely to attain a false alarm than HDA when hail is not observed. Other noteworthy performance improvements in HCA, relative to HDA, include a 33% increase in CSI and a 28% decrease in FAR. More detailed description of the results of this validation study can be found in Heinselman and Ryzhkov (2004).

**Rain–snow delineation.** Polarimetric properties of wet (melting) snow and snow crystals are very different from the ones in rain. Hence, these two snow categories are easily distinguishable from rain. However, discrimination between stratiform rain and dry ag-

**TABLE 3. Accuracy and skill measures of polarimetric (HCA) and conventional (HDA) algorithms over four hail events (47 reports), including probability of detection (POD), probability of false detection (POFD), false alarm rate (FAR), critical success index (CSI), and Heidke Skill Score (HSS). Accuracy measures range from 0% to 100%, whereas skill measures range from 0 to 1. Probabilities are rounded to the nearest integer.**

Algorithm	POD	POFD	FAR	CSI	HSS
HCA	100	25	11	0.89	0.80
HDA	88	58	39	0.56	0.31

gregated snow is a major challenge. Both classes are characterized by relatively low  $Z$  and  $Z_{DR}$ , combined with high  $\rho_{hv}$  (Ryzhkov and Zrníc 1998). Furthermore, there is no distinction in terms of the texture of the  $Z$  and  $\Phi_{DP}$  fields.

Figure 8 illustrates a scatterplot of  $Z$  versus  $Z_{DR}$  obtained from measurements with the KOUN radar for three different types of snow. Dry aggregated snow was observed on 6 February 2003 between 1500 and 1600 UTC over the entire state of Oklahoma. Seven hours later, dry aggregated snow changed to more crystallized snow in the very cold air northwest of the radar. It was characterized by much higher  $Z_{DR}$  and lower  $Z$ . Heavy convective snowfall occurred on 24 February 2003 in southern Oklahoma. Radar reflectivities over 50 dBZ are unusually high for snow in the latter case, but corresponding values of  $Z_{DR}$  are relatively low when compared to the ones typically observed at the bottom of the bright band. It is evident that data from rain and snow are heavily overlapped in the  $Z$ - $Z_{DR}$  plane for reflectivities between 20 and 40 dBZ. There is no clear distinction between these two classes in  $K_{DP}$  and  $\rho_{hv}$  as well. A clue for successful discrimination between these classes lies in the fact that stratiform rain and aggregated snow are usually separated by the melting layer (or bright band), which has very pronounced polarimetric signatures and can be easily detected. Therefore, rain/snow delineation is contingent upon the reliable identification of the melting layer.

In the current version of the classification algorithm, we detect the bottom of the melting layer by a sharp drop of the cross-correlation coefficient located slightly below local maxima in  $Z$  and  $Z_{DR}$  along the radial at the elevations between 4° and 9° in the direction away from the radar (Giangrande and Ryzhkov 2004). After the rain/snow delineation is made, only two classes, wet and dry snow, are distinguished at the snow altitudes/ranges. Correspondingly, no snow is allowed to occur in the rain region, that is, below the bright band (Ryzhkov and Zrníc 2003; Giangrande and Ryzhkov 2004).

An example of rain/snow transition for the

4 December 2002 freezing rain event is shown in Figs. 9 and 10. Brightband signatures are well pronounced in all three radar variables,  $Z$ ,  $Z_{DR}$ , and  $\rho_{hv}$  in the northern direction (Fig. 9). The area identified as rain has a very asymmetric form with respect to the radar (Fig. 10, bottom panel). The height of the melting level in the northwest sector is about 3 times lower than in the southwest sector of the radar coverage area. This signifies the passage of a cold front from the northwest. Note that the cross-correlation coefficient resumes its high values in dry snow above/beyond the bright band. Rain in the northwest sector ( $X$  between -60 and 0 km and  $Y$  between 0 and 60 km) was associated with subfreezing surface temperatures (Fig. 10) that resulted in raindrops freezing upon impact on the ground. This freezing rain caused hazardous road conditions and significant property damage in the Oklahoma City metropolitan area.

The height of the melting layer in the northern sector changes gradually because of the passage of a cold front (Fig. 10). Although surface temperatures did not change much during the 9-h period (except the portions of the north and northwest sectors far from the radar), the melting layer descended significantly to

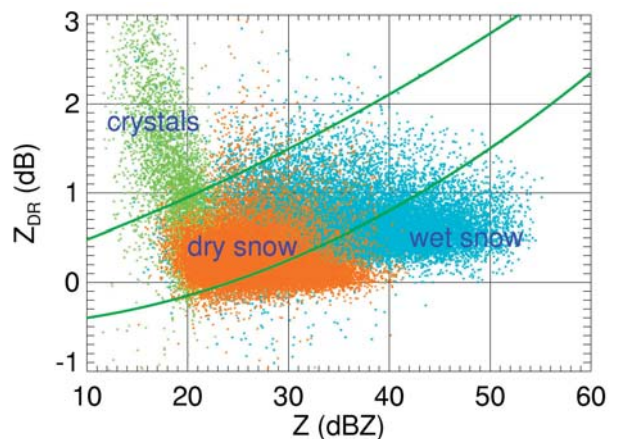


**FIG. 8. The  $Z$ - $Z_{DR}$  scatterplots for different types of snow. Two curves confine the area where the majority of the cold-season rain  $Z$ - $Z_{DR}$  pairs are usually observed.**

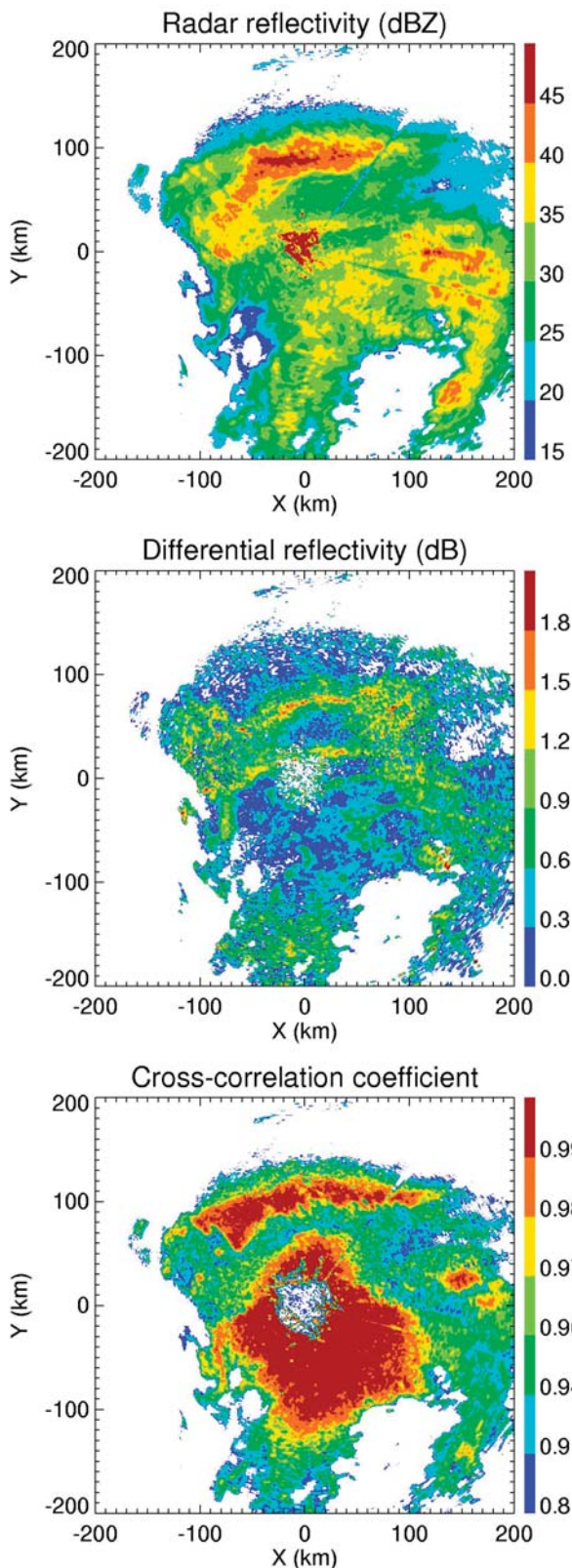


**FIG. 9.** Composite plot of  $Z$ ,  $Z_{DR}$ ,  $\rho_{hv}$ , at  $EI = 0.5^\circ$  at 0302 UTC 4 Dec 2002.

the north of the radar. This horizontal nonuniformity associated with the frontal boundary aloft is almost

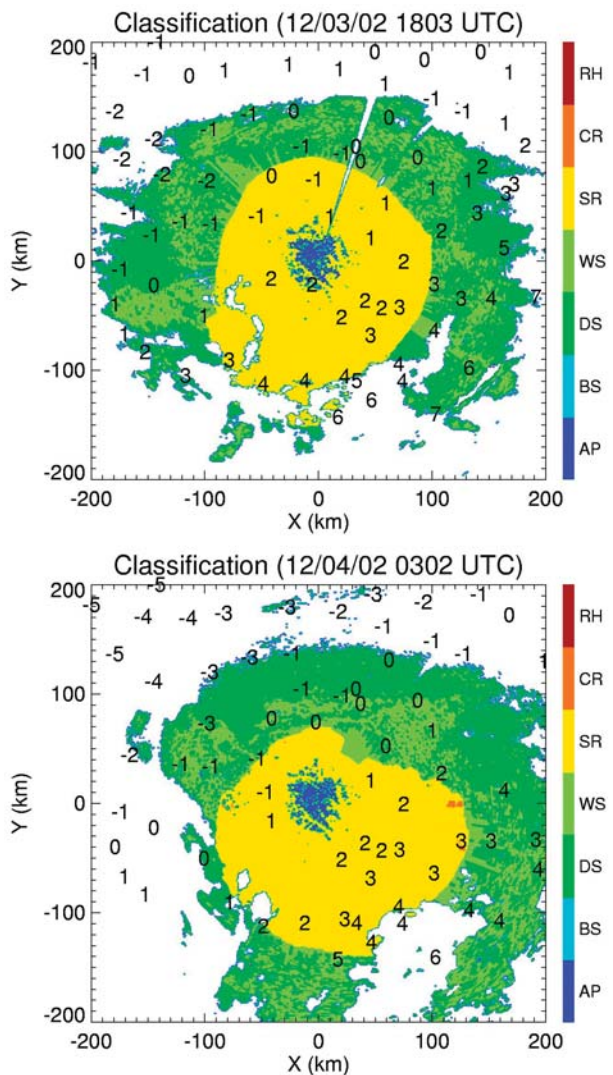


**FIG. 10.** Evolution of rain/snow boundary for the freezing rain event at the lowest radar scan ( $EI = 0.5^\circ$ ). AP stands for ground clutter/anomalous propagation, BS for biological scatterers, DS for dry snow, WS for wet snow, SR for stratiform rain, CR for convective rain, and RH for rain/hail mixture. Overlaid numbers indicate surface temperatures ( $^\circ\text{C}$ ).

impossible to capture with operational soundings. Practical implications of the use of radar polarimetric information in winter storms by NWS forecasters during JPOLE are discussed by Scharfenberg and Maxwell (2003), Miller and Scharfenberg (2003), and Scharfenberg and Lakshmanan (2004).

*Tornado detection.* Previous research with the NSSL Cimarron radar (Ryzhkov et al. 2002) led to the discovery of a polarimetric tornado signature associated with the Chickasha tornado (qualified as F3 on the Fujita scale) on 3 May 1999. The signature at the tip of the hook echo of that storm was characterized by  $Z_{DR}$

close to 0 dB and anomalously low  $\rho_{hv}$  (less than 0.5). Ryzhkov et al. (2002) concluded that the signature is attributed to randomly oriented nonmeteorological scatterers with irregular shapes and high refractive indexes (i.e., tornado debris).

As part of JPOLE, considerable KOUN data were acquired in tornadic storms. In particular, several damaging tornadoes occurred near the KOUN radar in May 2003. Most notable were the afternoons and evenings of 8 and 9 May when violent F4 and F3 tornadoes struck the Oklahoma City metropolitan area. In addition, several weaker tornadoes were observed during 6 days in April and May 2003.

Figure 11 shows a combined plot of  $Z$ ,  $Z_{DR}$ , and  $\rho_{hv}$  observed with the KOUN WSR-88D radar at the elevation of  $1.5^\circ$  at 2229 UTC (1729 CT) 8 May 2003 when the F4 tornado was reported. The tornado touchdown signature at the very tip of the hook is marked with  $Z_{DR}$  close to 0 dB and  $\rho_{hv} < 0.5$  (red arrows). A very similar signature was identified for the F3 tornado on 9 May 2003. In both cases, the location of the tornadic debris signature was consistent with damage paths obtained from a ground survey.

Examination of these three significant tornadic storms by Schuur et al. (2004; including the one on 3 May 1999) reveals a repetitive polarimetric tornado signature for strong tornadoes (F3 or higher on the Fujita scale). A cursory analysis of other tornadic storms indicates that the majority of the weak tornadoes did not produce definable signatures. One possible reason is that wind speeds in weak tornadoes are insufficient to significantly damage structures and loft debris. Another possible reason is that some of the weaker tornadoes may be too short lived; therefore, a debris signature might be missed because of coarse temporal sampling.

Based on these results, we believe that polarization measurements provide useful complementary information that can be used with the Doppler variables for mesocyclone and tornado detection. Doppler measurements require good spatial resolution to resolve the small tornadic vortex signature, whereas identification of polarimetric signatures may be accomplished with a coarser resolution. Moreover, these signatures are isotropic in nature, similar to Doppler velocity signatures of vortices, that is, they do not depend on a viewing angle.

In cases where traditional Doppler tornado-warning signatures are absent or overlooked by forecasters, the polarization tornado signature might be very valuable in preventing what otherwise might have been a missed warning. This signature might also be very helpful in issuing accurate severe weather-warning

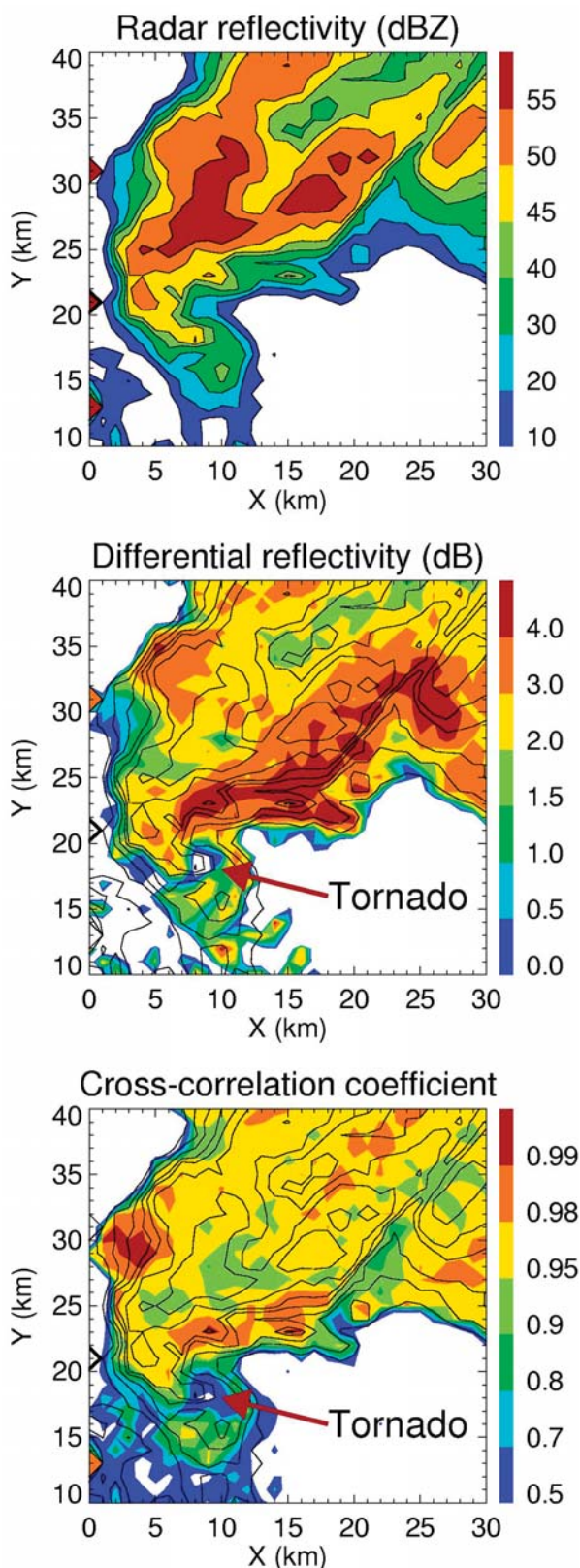


FIG. 11. Composite plot of  $Z$ ,  $Z_{DR}$ ,  $\rho_{hv}$ , for the Moore/Southeast Oklahoma City tornado on 8 May 2003 (2228 UTC, EI =  $1.5^\circ$ ). The tornado signature in  $Z_{DR}$  and  $\rho_{hv}$  is at the tip of the hook echo ( $X = 9$  km,  $Y = 18$  km).

updates to pinpoint the current tornado location and confirm the occurrence of damage (based on debris). Additional data analysis is required to examine the evolution of the 3D pattern of polarimetric variables prior to tornado touchdown and to possibly identify features that might serve as tornado precursors (Ryzhkov et al. 2005).

**SUMMARY.** The Joint Polarization Experiment (JPOLE) was designed to test the practicality and utility of a polarimetric WSR-88D radar. Highly successful data collection during JPOLE has provided a large dataset that is used to demonstrate the advantages of dual-polarization radar. It has demonstrated potential for significant improvement in areal rainfall estimation and measurements of heavy precipitation. Also, the unique classification capability based on polarimetric data has been confirmed to identify non-meteorological echoes (ground clutter/AP, insects, birds, and chaff) and improve hail detection.

Analysis of stratiform rain events and winter storms indicates that the operational polarimetric radar can be efficiently used to detect the bright band and delineate rain and snow. Discrimination between rain and snow at the lowest radar scan is necessary

to correctly estimate amounts of precipitation (liquid or frozen). Combined use of polarimetric data and surface temperatures is promising for the identification of freezing rain.

Validation of the polarimetric KOUN radar rainfall estimation and echo classification during JPOLE yielded very positive results, confirming the high quality of the polarimetric radar data and the viability of the simultaneous transmission/reception scheme. Although linear depolarization ratio (LDR), a traditional polarimetric variable, was not measured in the SHV mode, it appears that the absence of LDR does not compromise the quality of hydrometeor classification.

**ACKNOWLEDGEMENTS.** The authors would like to acknowledge funding support for this work from the U.S. National Weather Service, the Federal Aviation Administration, and the Air Force Weather Agency through the NEXRAD Product Improvement Program. Additional funding came from the National Science Foundation Grant ATM-9907930. The upgrades of the KOUN WSR-88D radar were implemented under the leadership of Allen Zahrai.

**APPENDIX A: RADAR RAINFALL RELATIONS.** As a basic conventional algorithm for radar rainfall estimation, we use the standard NEXRAD  $R(Z)$  relation

$$R(Z) = 1.70 \cdot 10^{-2} Z^{0.714}, \quad (A1)$$

where  $Z$  is expressed in  $\text{mm}^6 \text{m}^{-3}$  and  $R$  in  $\text{mm h}^{-1}$ . Values of  $Z$  are limited to a maximum of 53 dBZ to mitigate hail contamination.

We have tested 19 different polarimetric algorithms, including the most recent  $R(K_{\text{DP}})$ ,  $R(Z, Z_{\text{DR}})$ , and  $R(K_{\text{DP}}, Z_{\text{DR}})$  S-band power-law relations found in literature and algorithms that we derived using multiyear statistics of DSD measurement in central Oklahoma (with different assumptions about raindrop shape-size dependencies). A full list of these algorithms is presented by Ryzhkov et al. (2003a).

Combining the merits of different algorithms for various rain intensities, we developed a “synthetic” algorithm  $R(Z, K_{\text{DP}}, Z_{\text{DR}})$  that uses different combinations of radar variables depending on the rain rate estimated with the conventional  $R(Z)$  relation. The following is a description of the proposed algorithm (Ryzhkov et al. 2003a,b):

If  $R(Z) < 6 \text{ mm h}^{-1}$ , then

$$R = R(Z)/(0.4+5.0 |Z_{\text{dr}} - 1|^{1.3}); \quad (A2)$$

if  $6 < R(Z) < 50 \text{ mm h}^{-1}$ , then

$$R = R(K_{\text{DP}})/(0.4+3.5 |Z_{\text{dr}} - 1|^{1.7}); \quad (A3)$$

if  $R(Z) > 50 \text{ mm h}^{-1}$ , then  $R = R(K_{\text{DP}})$ , where

$$R(K_{\text{DP}}) = 44.0 |K_{\text{DP}}|^{0.822} \text{sign}(K_{\text{DP}}). \quad (A4)$$

In (A2)–(A4),  $Z_{dr}$  is differential reflectivity expressed in linear units [ $Z_{DR}(\text{dB}) = 10 \log(Z_{dr})$ ], and  $K_{DP}$  is in  $\text{deg km}^{-1}$ .

The  $R(Z, K_{DP}, Z_{DR})$  algorithm is structured in such a way that the combination of  $K_{DP}$  and  $Z_{DR}$  is used for estimation of about half of all rainfall in Oklahoma (according to the DSD statistics). It is known from simulations that, compared to the  $R(Z)$ ,  $R(K_{DP})$ , and  $R(Z, Z_{DR})$  relations, the  $R(K_{DP}, Z_{DR})$  algorithm is least affected by DSD variations and uncertainties in raindrop shapes and canting angles. At lower rain rates ( $< 6 \text{ mm h}^{-1}$ ), the combination of  $K_{DP}$  and  $Z_{DR}$  is less efficient because  $K_{DP}$  becomes too noisy, therefore,  $Z$  (instead of  $K_{DP}$ ) should be used jointly with  $Z_{DR}$ . For very high rain rates ( $> 50 \text{ mm h}^{-1}$ ), both  $Z_{DR}$  and  $Z$  are very likely contaminated with hail, and the synthetic algorithm relies exclusively on  $K_{DP}$ . Another advantage of such an approach is that reflectivity calibration is required only for light rain (with intensity less than  $6 \text{ mm h}^{-1}$ ), which accounts for about 32% of the annual rain in Oklahoma according to multiyear statistics of disdrometer measurements.

**APPENDIX B: ACCURACY AND SKILL SCORES.** The  $2 \times 2$  contingency tables were constructed by comparing algorithm detections to ground truth, where  $a$  is a hit,  $b$  is a false alarm,  $c$  is a miss, and  $d$  is a correct null. For each case, and all cases combined, we examined three accuracy measures, including probability of detection (POD), where

$$\text{POD} = \frac{a}{a+c}; \quad (\text{B1})$$

probability of false detection (POFD), where

$$\text{POFD} = \frac{b}{b+d}; \quad (\text{B2})$$

$$\text{FAR} = \frac{b}{a+b}; \quad (\text{B3})$$

and critical success index (CSI), where

$$\text{CSI} = \frac{a}{a+b+c}. \quad (\text{B4})$$

Each of these measures ranges from 0 to 1, though POD and POFD are typically expressed in terms of percentages. A perfect forecast would have a POD of 100%, a POFD of 0%, and a CSI of 1. Additionally, we examined the Heidke skill score (HSS),

$$\text{HSS} = \frac{2(ad-bc)}{(a+c)(c+d) + (a+b)(b+d)}. \quad (\text{B5})$$

## REFERENCES

- Aydin, K., T. A. Seliga, and V. Balaji, 1986: Remote sensing of hail with a dual linear polarization radar. *J. Climate Appl. Meteor.*, **25**, 1475–1484.
- Balakrishnan, N., and D. S. Zrnica, 1990: Estimation of rain and hail rates in mixed-phase precipitation. *J. Atmos. Sci.*, **47**, 565–683.
- Bringi, V. N., and V. Chandrasekar, 2001: *Polarimetric Doppler Weather Radar: Principles and Applications*. Cambridge University Press, 636 pp.
- Brock, F. V., K. C. Crawford, R. L. Elliott, G. W. Cuperus, S. J. Stadler, H. L. Johnson, and M. D. Eilts, 1995: The Oklahoma Mesonet: A technical overview. *J. Atmos. Oceanic Technol.*, **12**, 5–19.
- Doviak, R. J., and D. S. Zrnica, 1993: *Doppler Radar and Weather Observations*. 2d ed. Academic Press, 562 pp.
- , V. Bringi, A. V. Ryzhkov, A. Zahrai, and D. S. Zrnica, 2000: Considerations for polarimetric upgrades to operational WSR-88D radars. *J. Atmos. Oceanic Technol.*, **17**, 257–278.
- , J. K. Carter, V. M. Melnikov, and D. S. Zrnica, 2002: Modifications to the research WSR-88D to obtain polarimetric data. National Severe Storms Laboratory Rep., 49 pp.

- Giangrande, S. E., and A. V. Ryzhkov, 2004: Polarimetric method for bright band detection. Preprints, *11th Conf. on Aviation, Range, and Aerospace Meteorology*, Hyannis, MA, Amer. Meteor. Soc., CD-ROM, P5.8.
- Heinselman, P. L., and A. V. Ryzhkov, 2004: Hail detection during the Joint Polarization Experiment. Preprints, *22nd Conf. on Severe Local Storms*, Hyannis, MA, Amer. Meteor. Soc., CD-ROM, J1.3.
- Liu, H., and V. Chandrasekar, 2000: Classification of hydrometeors based on polarimetric radar measurements: Development of a fuzzy logic and neuro-fuzzy systems, and in situ verification. *J. Atmos. Oceanic Technol.*, **17**, 140–164.
- Miller, D. J., and K. A. Scharfenberg, 2003: The use of polarimetric radar data in the winter weather warning decision making process: A case study. Preprints, *31st Int. Conf. on Radar Meteorology*, Seattle, WA, Amer. Meteor. Soc., 976–979.
- Ryzhkov, A. V., and D. S. Zrnica, 1996: Rain in a shallow and deep convection measured with a polarimetric radar. *J. Atmos. Sci.*, **53**, 2989–2995.
- , and —, 1998: Discrimination between rain and snow with a polarimetric radar. *J. Appl. Meteor.*, **37**, 1228–1240.
- , and —, 2003: Discrimination between rain and snow with a polarimetric NEXRAD radar. Preprints, *31st Int. Conf. on Radar Meteorology*, Seattle, WA, Amer. Meteor. Soc., 635–638.
- , D. W. Burgess, D. S. Zrnica, T. Smith, and S. E. Giangrande, 2002: Polarimetric analysis of a 3 May 1999 tornado. Preprints, *21st Conf. on Severe Local Storms*, San Antonio, TX, Amer. Meteor. Soc., 515–518.
- , S. E. Giangrande, and T. J. Schuur, 2003a: Rainfall measurements with the polarimetric WSR-88D radar. National Severe Storms Laboratory Rep., 98 pp.
- , —, and —, 2003b: Rainfall estimation with a polarimetric prototype of the operational WSR-88D radar. Preprints, *31st Int. Conf. on Radar Meteorology*, Seattle, WA, Amer. Meteor. Soc., 208–211.
- , T. J. Schuur, D. W. Burgess, and D. S. Zrnica, 2005: Polarimetric tornado detection. *J. Appl. Meteor.*, in press.
- Scharfenberg, K. A., and E. Maxwell, 2003: Operational use of a hydrometeor classification algorithm to detect the snow melting level. Preprints, *31st Int. Conf. on Radar Meteorology*, Seattle, WA, Amer. Meteor. Soc., 639–641.
- , and V. Lakshmanan, 2004: The use of NWP data in polarimetric hydrometeor classification. Preprints, *11th Conf. on Aviation, Range, and Aerospace Meteorology*, Hyannis, MA, Amer. Meteor. Soc., CD-ROM, P5.7.
- Schuur, T. J., A. V. Ryzhkov, P. L. Heinselman, D. S. Zrnica, D. W. Burgess, and K. A. Scharfenberg, 2003: Observations and classification of echoes with the polarimetric WSR-88D radar. National Severe Storms Laboratory Rep., 46 pp.
- , —, D. W. Burgess, and D. S. Zrnica, 2004: Polarimetric radar observations of tornadic debris signatures. Preprints, *22nd Conf. on Severe Local Storms*, Hyannis, MA, Amer. Meteor. Soc., CD-ROM, 8B.3.
- Seo, D. J., J. Breidenbach, R. A. Fulton, D. Miller, and T. O'Bannon, 2000: Real-time adjustment of range-dependent biases in WSR-88D rainfall estimates due to nonuniform vertical profile of reflectivity. *J. Hydrometeorol.*, **1**, 222–240.
- Smith, J. A., D. J. Seo, M. L. Baeck, and M. D. Hudlow, 1996: An intercomparison study of NEXRAD precipitation estimates. *Water Resour. Res.*, **32**, 2035–2045.
- Smyth, T. J., T. M. Blackman, and A. J. Illingworth, 1999: Observations of oblate hail using dual polarization radar and implications for hail-detection schemes. *Quart. J. Roy. Meteor. Soc.*, **125**, 993–1016.
- Straka, J. M., D. S. Zrnica, and A. V. Ryzhkov, 2000: Bulk hydrometeor classification and quantification using multiparameter radar data. Synthesis of relations. *J. Appl. Meteor.*, **39**, 1341–1372.
- Vivekanandan, J., D. S. Zrnica, S. M. Ellis, R. Oye, A. V. Ryzhkov, and J. M. Straka, 1999: Cloud microphysics retrieval using S-band dual-polarization radar measurements. *Bull. Amer. Meteor. Soc.*, **80**, 381–388.
- Witt, A., M. D. Eilts, G. J. Stumpf, J. T. Johnson, E. D. Mitchell, and K. W. Thomas, 1998: An enhanced hail algorithm for the WSR-88D. *Wea. Forecasting*, **13**, 286–303.
- Zhang, P., A. V. Ryzhkov, and D. S. Zrnica, 2004: Detection of birds and insects using polarimetric radar observations. Preprints, *11th Conf. on Aviation, Range, and Aerospace Meteorology*, Hyannis, MA, Amer. Meteor. Soc., CD-ROM, P5.13.
- Zrnica, D. S., and A. V. Ryzhkov, 1996: Advantages of rain measurements using specific differential phase. *J. Atmos. Oceanic Technol.*, **13**, 454–464.
- , and —, 1998: Observations of insects and birds with a polarimetric radar. *IEEE Trans. Geosci. Remote Sens.*, **36**, 661–668.
- , and —, 1999: Polarimetry for weather surveillance radars. *Bull. Amer. Meteor. Soc.*, **80**, 389–406.
- , and —, 2004: Polarimetric properties of chaff. *J. Atmos. Oceanic Technol.*, **21**, 1017–1024.
- , —, J. M. Straka, Y. Liu, and J. Vivekanandan, 2001: Testing a procedure for automatic classification hydrometeor types. *J. Atmos. Oceanic Technol.*, **18**, 892–913.